ChemComm

COMMUNICATION

View Article Online
View Journal | View Issue

Cite this: *Chem. Commun.*, 2022, **58**, 9092

Received 16th June 2022,
Accepted 20th July 2022

DOI: 10.1039/d2cc03368b

rsc.li/chemcomm

Velocity map images from surface-hopping; reactive scattering of OH ($^2\Sigma^+$) + H_2 ($^1\Sigma_g^+$)†

Christopher Robertson * and Martin J. Paterson

We study OH(Σ) + H_2 → $H_2O(X)$ + H reactive scattering using two potential energy models found in the literature. We analyze the quenching channels and generate velocity map images (VMI) by simulating quantum-classical trajectories of the quenched products. The initial conditions attempt to simulate supersonic jet, molecular beam scattering experiments which we compare against. The simulated results are able to elucidate the mechanisms behind some of these experimental observations.

The Hydroxyl radical, a key oxidizing agent in atmospheric and combustion processes, has been the subject of intense experimental study.[1–4] The presence of this radical is often monitored using Laser-induced fluorescence on the $A^2\Sigma^+$–$X^2\Pi$ band system. The electronically excited species can lead to significant energy release *via* quenching, as is the case with the Hydrogen molecule, where two competing quenching channels are available; OH(Σ^+) + H_2 → OH(Π) + H_2 (non-reactive) or → H_2O + H (reactive). Understanding the impact of this process in the OH(Σ^+) lifetime is of importance. A complementary body of theoretical work has been also taken place,[5–8] given the rich experimental data available. Much of this work culminated in two analytic models by Truhlar *et al.*[6] and Yarkony *et al.*,[7] and have more recently been used to perform dynamic simulations with them (Guo *et al.*[8,9]) to estimate a number of observables.

In this communication we generate velocity map images (VMI) and H product distributions, previously omitted.[8,9] Velocity Map imagining is a mature and popular method for obtaining simultaneous angles and velocities (and a wealth of other implicit information) from scattering experiments.[10] The popularity of this method makes it a natural choice for computational scientist to simulate, to effectively communicate results with experimentalist. We performed semi-classical trajectories on the potential energy surface (PES), used in similar systems to study quenching[11,12] and angular and velocity distributions.[13–16] Numerical quantum mechanical propagation and integration of these equations is a computationally intensive and hard to generalize. In contrast, for semi-classical trajectories the evaluation of velocity and scattering angles of particles can be done irrespective of the size of the system, using uniform phase-space binning procedures.[17,18] Crossed-beams experimental work by Ortiz-Suarez *et al.*[4] was done on the OH + D_2 → HOD + D and obtained center of mass velocity map images from simulations fitted to experimental data. Also related, Lester *et al.*[19,20] have performed Doppler profile measurements for the reaction products of these isotopically analogous systems under similar conditions. Finally, Brouard *et al.* have recently measured absolute cross-sections for the competing channels for this system, as well as several other experimental observables.[3] Although this system is prototypical, being small and with competitive quenching channels, the PES description is nevertheless challenging. Although the models emphasize different mechanistic aspect of the scattering process, they are able to provide rich insight into some of the aforementioned experiments.

Two model PES are used here. A four-state diabatic PES developed by Malbon, Zhao, Guo and Yarkony (MZGY)[7] and a three-state diabatic model developed by Shu, Bowman and Truhlar *et al.* (FWW2).[8] At certain OH/H_2 distances beyond 2.5 Å we found in FWW2 a discontinuity of the OH stretch PE; at such distances we switched to FWW1,[6] which matches FWW2 in most regions of the PES. Some PES cuts and couplings are provided in ESI.† Intersection seams connect the S_2/S_1 and S_2/S_0 along the H_2 rotation in a planar configuration,[6,7] where most quenching is expected.

We employed the SHARC code[21] to integrate the equations of motion, in the adiabatic representation, using the fewest-switches algorithm[22] on the non-adiabatic coupling provided by the models. We also applied energy based decoherence[23] and post-hopping parallel velocity rescaling (further details in ESI†).

School of Engineering & Physical Sciences, Heriot-Watt University, Edinburgh, Scotland EH14 4AS, UK. E-mail: m.j.paterson@hw.ac.uk

† Electronic supplementary information (ESI) available: Simulated data for FWW1 model, PES, and rovibrational spectrum. See DOI: https://doi.org/10.1039/d2cc03368b

The internal and rotational degrees of freedom (DOF) are in their ground state. Given the afforded trajectories (~25k per model) compared to similar examples[13,15] we sample the orientations in fixed lattice points (used a Fibonacci sphere). We used 16 lattice points for OH and 9 for H_2. For similar reasons we used regular lattice points for sampling the impact parameter (IP) b, spanning 10 bohr (9 lattice points). We used the Wigner distribuition obtained from the numerical integration of the stretch mode for each diatom (far from each other). These distributions where then sampled using Monte Carlo (MC) (16 samples per lattice point). Because this is a form of biased sampling (towards low IP), we weight the trajectories when constructing the resulting observables by the cross sectional area approximated by the bin width of that lattice point. An additional thousand trajectories were added to high IP lattice points. This results in 25k trajectories per model. A collisional energy of 0.05 eV was used, within a few factors of several experimental results discussed in the Discussions.

All trajectories were integrated until outgoing molecules where at least 6 Å apart. Approximately 2.5% of FWW2 trajectories lead to excessive energy changes during integration. Further detailed images, such as ro-vibrational spectra are offered as ESI,† as well as results for the FWW1 model.

Fig. 1 shows the branching ratio for the different channels for both models. The non-quenching channels are dominant and the quenched channels decrease as a function of IP. Integrating the bins that contain some quenching, we get 92% (MZGY) and 86% (FWW2) of the cross section results in non-quenching. Of the quenching channels, the non-reaction channel is 3.8 (MZGY) and 4.1 (FWW2) times greater than the reaction channel. By defining a OH/H_2 intermolecular incoming distance of 2.5 Å and outgoing distance 4.0 Å as cutoffs to measure the mean lifetime of the interacting complex. We found 155 (MZGY)/164 (FWW2) fs for non-reactive, 165/178 fs for reactive and 167/360 fs for OH nascent H. For FWW2, the incident H-facing OH (facing the incoming H_2) compared to O-facing OH, has three times the expected lifetime (ESI† for details). Fig. 2 provides some insight into the initial quenching mechanisms by plotting the number of *first instance* hopping events weighted by the cross section as a function of the angle between the OH and H_2 bond vectors, θ. The H_2 vector is defined as always pointing away from the Oxygen. Zero degrees corresponds to the O-facing OH (facing the incoming H_2), while 180° to H-facing OH. Each cells show the differential cross section as a function of θ for $S_2 \rightarrow S_1 \mid S_0$ and $S_1 \rightarrow S_0$ transitions for the non-reaction (NR) and reaction channels (Rx). The *first instance* of a state transition (hop) from either transitions $S_2 \rightarrow S_1 \rightarrow S_0$ or $S_1 \rightarrow S_0$ is used.

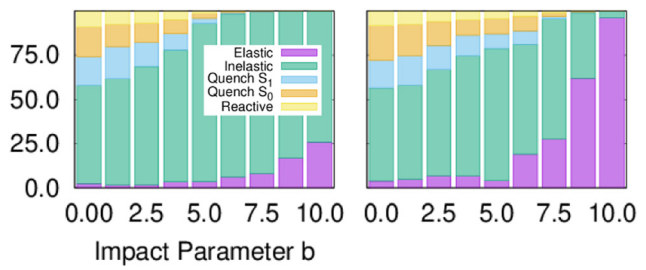

Fig. 1 Branching ratios for the different channels as a function of impact parameter, models MZGY (left) and FWW2 (right).

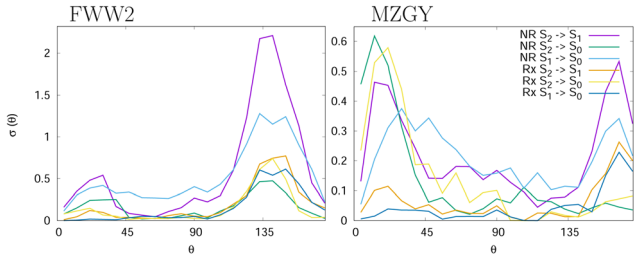

Fig. 2 Differential cross section as a function of the angle between the OH and H_2 bond vectors as described in text, at the first instance of quenching for 6 different channels: Non Reactive (NR) from $S_2 \rightarrow S_1$ (purple), $S_2 \rightarrow S_0$ (green), $S_1 \rightarrow S_0$ (light-blue); non reactive (NR) from $S_2 \rightarrow S_1$ (orange), $S_2 \rightarrow S_0$ (yellow), $S_1 \rightarrow S_0$ (dark-blue).

Both models suggest that quenching from the S_2 (Σ) state occur preferentially at acute and obtuse angles. For MZGY, first $S_2 \rightarrow S_0$ hop represent the largest cross section, and occur primarily at acute angles 15–20° (O-facing H_2). $S_2 \rightarrow S_1$ in contrast occurs at wider angles ≈160°, while $S_1 \rightarrow S_0$ has a broad distribuition across all angles. The FWW2 model in contrast exhibits preferred hops at wide angles (H-facing OH) at ≈145° for most transitions, with exception to $S_1 \rightarrow S_0$ which is also broad. A second minor peak at low acute angles is also present. ESI† offers more detailed images of the same account.

Fig. 3 shows the simulated velocity map images obtained from both models for the quenched H_2 and H products. Zero degrees corresponds to the forward scattering hydrogens, in the same direction as the Hydrogen molecule's initial (z) velocity vector direction. The forward ("F") and backward ("B") fraction, as defined by the amount less or greater than π/2 angle respectively, is also shown in the figure. The red scattered

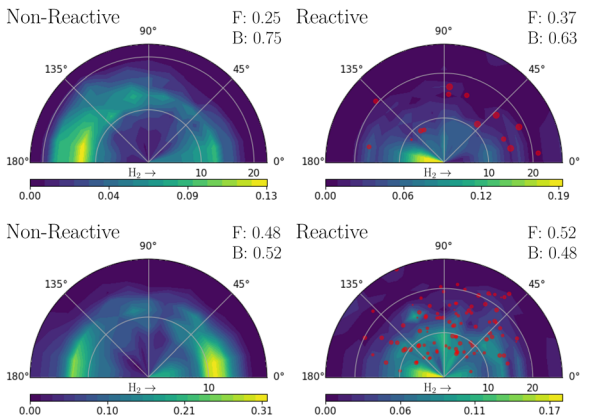

Fig. 3 Velocity Map images of the quenched H_2 (left) or H product (right) from the reactive quenching channel in the MZGY (upper) and FWW2 (lower) models. The "F" and "B" labels describe the cross section fraction in the "Forward" ($<\pi/2$) or "Backward" ($>\pi/2$) directions. The red scattered points in the plot show the OH nascent H atoms, with a size proportional to their cross-section weight.

points show the OH nascent H atoms, with a size proportional to their cross-section weight; these are ~2% of H atoms in MZGY (21 trajectories), and 13% in FWW2. The VMI for IP greater (less) than 3 Å are provided as ESI,† and show an expectedly dominant forward (backward) distribuition. Forward scattering H products have a higher velocity; trajectories with angles $<\pi/2$ have an average of 14.5 (MZGY) 14.3 (FWW2) km s^{-1} compared to 12.8 (MZGY) 13.3 (FWW2) km s^{-1} for angles $> \pi/2$. By the time H_2O and Hydrogen are away from the interaction region, the internal energy distribution of water is very similar for all 3 DOF and rotational energy. The mean H velocity as a function of b does not change substantially (~12 km s^{-1} for MZGY, 13–15 km s^{-1} for FWW2). The spread of velocities is broad (see below), contrasting with the H_2 maps, which exhibit in both models a high translational energy release. MZGY suggests an overall dominant backwards scattering of H_2 (75% of H_2 $< \pi/2$) and H (63%). In contrast, FWW2 slightly favours forward scattered H products (52%) while slight backward for H_2 (52%). MZGY OH nascent H products favor a forward scattered angle, with a mean angle of 76° (80% occurring at low, <2.5 a_0, IP) in contrast to a more isotropic distribution for FWW2 of 89° (a broader range of IP).

Fig. 4 shows the H product Kinetic Energy (KE) distribution of both models, with the distribution of OH nascent H atoms in green. Both models are qualitatively similar, with exception to the OH nascent H product, which for MZGY the maxima lies around 1.5 eV (modest number of 21 samples).

Fig. 1 is semi-quantitatively similar to that found by ref. 8, for both models. By integrating until the last bin containing quenching trajectories, the non-quenching channels represent at least 86% of the cross section. This dominant non-quenching channel qualitatively agrees with experimental work by Brouard *et al.*;[3] nevertheless, they suggests an approximate 3 : 1 ratio. One can expect that inclusion of Renner–Teller coupling, neglected by these models, would lead to an significant increase quenching further by a substantial factor, potentially putting in closer in line with experiments.[11] The non-reaction channel is 3.8 (MZGY) and 4.1 (FWW2) times greater than the reaction channel, which is agreement with Collins *et al.*[5] This contrasts with earlier estimated results by Lester *et al.*[20,24] suggesting the opposite trend. Nevertheless, as argued elsewhere,[9] their estimate was based on a poor estimate of the size of non-quenching channels; upon correction,[3] the non-reaction channel becomes the dominant one. The reaction branching ratio decays more rapidly as a function of b in the MZGY model, making strongly forward scattered H product less likely (in contrast to the FWW2), as observed in Fig. 3.

The near co-linear $C_{\infty\nu}$ geometries are favored as the dominant quenching channel agrees with previously reported results.[8,9] There is a long range (dipole-quadrapole) interaction at linear or perpendicular to H_2 orientations depending on the atom OH face. Quenching in FWW2 model strongly prefers H-facing OH entrance channel which also dominates the mechanism leading the production of Hydrogen (Fig. 2). This is in disagreement with the recent simulations,[8] which imply the opposite results. Its worth noting they used six times greater collisional energies. The long range potential is determined by FWW1, and although semi-quantitatively similar to FWW2, may well be over-emphasizing this channel. When hopping, the OH_3 complex tends to form a rhombus complex structure with the oxygen at a long end, consistent with an angle of ≈145° (Fig. 2). In such orientations, $S_2 \rightarrow S_1$ is the largest quenching channel (FWW2); from there, the broad distribuition of angles for $S_1 \rightarrow S_0$ (for both models) show that by the time the transition takes place the H_2 has already formed a chaotic, energetic complex with all hydrogens exchanging. The lifetime of incident H-facing OH complexes is estimated nearly 3 times greater than O-facing (see ESI†), increasing quenching. The MZGY model also shows this attractive entrance channel with H-facing hydroxide, but the dynamic steering effect is weaker, complex lifetime shorter (compared with FWW2), non-adiabatic coupling is comparatively absent (see ESI†) and consequently is not a dominant channel (Fig. 2). The $S_2 \rightarrow S_0$ direct transfer to the ground state occurs largely at O-facing OH geometries. Particularly for MZGY, also being the mechanism for the OH nascent H product (see below).

A OH + D_2 cross-beam VMI image by Ortiz-Suárez *et al.*[4] is reproduced as ESI.† Mean collision energies are estimated at ≈0.16 eV, three times higher than in the simulations presented here. They observed two H product velocity distributions; a (likely low b) backward scattered channel representing 25% of the cross-section, and a dominant forward channel (75%). The KE distribuition of both channels are similar, peaking ≈0.5 eV with a long tail to the maximum available energy (≈4 eV), in broad agreement with other work.[20] This is in qualitative disagreement with the MZGY and in only slight agreement with FWW2. Since forward scattering is clearly dominated by larger IP trajectories, the MZGY model may well not be characterizing the long range-interactions sufficiently. The OH nascent H product channel, which is largely forward scattered (Fig. 3) may also be underestimated. OH nascent H products of FWW2 arise from long-lived complexes, nearly twice as long as otherwise. This is a consequence of a strong randomization of the energy amongst the H atoms, which agrees with the models weak dependence of this processes as a function of IP, and the overall isotropic distribution. Visual inspection of trajectories also agrees with this assessment. Given the reactive cross section is most prominent for impact parameters $b < 6a_0$, the collisional energy results in a typical orbit period for the system in the range of hundreds (<800 fs) of femtoseconds; the ~160 fs the diatoms spend interacting is enough to result in an isotropic distribuition.

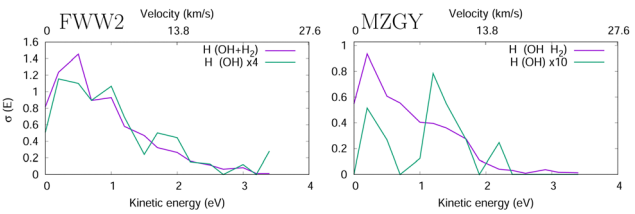

Fig. 4 H product kinetic energy distribution in the FWW2 (left) and MZGY (right) models. The OH nascent H product also shown (green).

Lester *et al.*[19,20] estimated two velocity distributions of the nascent H atoms with average KEs of 0.12 and 1.65 eV. OD + H_2 scattering result in 75% HOD and 25% H_2O products of the reaction cross section (60/40% for OH). The Nascent H atoms in OD + H_2 → H + HOD, have a low average KE peaking at 0.15 eV, 2/3 with less than 0.5 eV and a long 4 eV tail. In contrast the D + H_2O, product deuterium distribuition exhibits a second shoulder peaking at 1.8 eV, and more KE released into the translational DOF. This latter distribuition is naturally attributed to an insertion mechanism of the OH into the H2 molecule, likely at low IP. Collisional energies range in 0.005–0.05 eV, and appear qualitatively consistent.[19,20] Together, the models used here may be able to partially flesh out some of these observations. The MZGY only gave a very limited number of OH nascent H product trajectories. Most of these (>90%) can be described as a H_2 insertion mechanism and forward ejected OH nascent H product, which explains the second shoulder peak shown in Fig. 4. Although the OH nascent H product is underestimated by MZGY, it displays the correct channels when compared to experimental KE H product distributions.[20] Although such an insertion mechanism is also present in the FWW2 model results, these comprise a small number (<15%) of the reactions (1.8 eV shoulder is weakly apparent in Fig. 4. Instead, the majority of OH nascent H product trajectories start with the OH H atom pointing towards the H_2 (as discussed above); an attractive potential leads to a relatively long-lived ($10 < t < 70$ fs) configuration with all H_3 shuffling while the complex rotates (leading to the isotropic distribution observed in Fig. 3) explaining why it has a similar distribuition in Fig. 4 for the overall nascent H products. In contrast with MZGY, where the OH nascent H *via* the H-facing OH entrance channel mechanism appears as a very minor, with only 3 trajectories with incident H-facing OH. The distributions of H products with energies below 1 eV (the dominant higher peak) in experiments[20] could tentatively be assigned to the (incident H-facing) OH shuffling of H atoms in a long-lived complex. While the secondary, high energy peak can be attributed to the forward scattered OH nascent H product with a higher KE release *via* an insertion mechanism.

Two models, MZGY[9] FWW2[8] where used to simulate molecular beam scattering experiments. Velocity maps, branching ratios, channel cross sections and H-product translational distributions where estimated. Results for branching ratios and cross sections are in semi-quantitative agreement with previous simulations. Both suggest the non-quenching to be dominant, albeit more than experimentally measured.[3] The non-reactive channel is at least three times greater than the reactive channel, in agreement with experimental estimates.[9,20,24] The FWW2 favors quenching around a H-facing OH orientation, while MZGY only if it quenches *via* S_1 first (direct S_0 prefers O-facing incoming OH). Experiments[4] suggesting a dominant forward scattered H products is only modest agreement with FWW2 and weak disagreement with MZGY. Nevertheless, together both models describe reactive channels that might help explain the experimental observations. The models suggest that the low KE release of H is likely a result of energy redistribution during the (100–200 fs) lifetime of the OH_3 complex. This complex may form from the dynamical steering of the OH at either H or O-facing the H_2 molecule, the Hydrogen facing entrance channel leading to more chaotic behavior (more isotropic distribuition, and possibly, longer lived). An O-facing OH leads to a more likely insertion mechanism, with a higher KE release of the nascent H product, leading to the 1.8 eV second shoulder observed in experiments. This mechanism, as well as high impact parameter, abstraction reactions lead to a dominant forward scattered observed by experiments. Thanks to these models, the mechanism behind these experiments is beginning to come into focus.

Conflicts of interest

No conflicts of interest.

Notes and references

1 J. H. Lehman and M. I. Lester, *Ann. Rev. Phys. Chem.*, 2014, **65**, 537–555.
2 B. L. Hemming and D. R. Crosley, *J. Phys. Chem. A*, 2002, **106**, 8992–8995.
3 M. Brouard, J. Lawlor, G. McCrudden, T. Perkins, S. A. Seamons, P. Stevenson, H. Chadwick and F. J. Aoiz, *J. Chem. Phys.*, 2017, **146**, 244313–244323.
4 M. Ortiz-Suárez, M. F. Witinski and H. F. Davis, *J. Chem. Phys.*, 2006, **124**, 4–7.
5 M. A. Collins, O. Godsi, S. Liu and D. H. Zhang, *J. Chem. Phys.*, 2011, **135**, 234307–234314.
6 Y. Shu, J. Kryven, A. G. Sampaio De Oliveira-Filho, L. Zhang, G. L. Song, S. L. Li, R. Meana-Pañeda, B. Fu, J. M. Bowman and D. G. Truhlar, *J. Chem. Phys.*, 2019, **151**, 104311–104324.
7 C. L. Malbon, B. Zhao, H. Guo and D. R. Yarkony, *Phys. Chem. Chem. Phys.*, 2020, **22**, 13516–13527.
8 S. Han, A. G. de Oliveira-Filho, Y. Shu, D. G. Truhlar and H. Guo, *ChemPhysChem*, 2022, **23**, 10064–10101.
9 B. Zhao, S. Han, C. L. Malbon, U. Manthe, D. R. Yarkony and H. Guo, *Nat. Chem.*, 2021, **13**, 909–915.
10 J. N. Bull, J. W. Lee, S. H. Gardiner and C. Vallance, *Eur. J. Mass Spectrom.*, 2014, **20**, 117–129.
11 T. Perkins, D. Herráez-Aguilar, G. McCrudden, J. Kłos, F. J. Aoiz and M. Brouard, *J. Chem. Phys.*, 2015, **142**, 144307–144315.
12 H. Chadwick, M. Brouard, Y. P. Chang, C. J. Eyles, G. McCrudden, T. Perkins, S. A. Seamons, J. Kłos, M. H. Alexander, P. J. Dagdigian, D. Herráez-Aguilar and F. J. Aoiz, *J. Chem. Phys.*, 2014, **140**, 79–123.
13 S. J. Greaves, E. Wrede, N. T. Goldberg, J. Zhang, D. J. Miller and R. N. Zare, *Nature*, 2008, **454**, 88–91.
14 S. J. Greaves, R. A. Rose, F. Abou-Chahine, D. R. Glowacki, D. Troya and A. J. Orr-Ewing, *Phys. Chem. Chem. Phys.*, 2011, **13**, 11438–11445.
15 S. J. Greaves, D. Murdock, E. Wrede and S. C. Althorpe, *J. Chem. Phys.*, 2008, **128**, 0–10.
16 C. Huang, W. Li and A. G. Suits, *J. Chem. Phys.*, 2006, **125**, 133107–133109.
17 R. Bernstein, *Atom-molecule collision theory*, Plenum P., New York, 1979, ch. 16.
18 M. B. Faist, *J. Chem. Phys.*, 1976, **65**, 5427–5435.
19 D. T. Anderson, M. W. Todd and M. I. Lester, *J. Chem. Phys.*, 1999, **110**, 11117–11120.
20 J. H. Lehman, J. L. Bertrand, T. A. Stephenson and M. I. Lester, *J. Chem. Phys.*, 2011, **135**, 144303–144309.
21 S. Mai, M. Richter, M. Heindl, M. F. S. J. Menger, A. Atkins, M. Ruckenbauer, F. Plasser, L. M. Ibele, S. Kropf, M. Oppel, P. Marquetand and L. Gonzalez, *SHARC2.1: Surface Hopping Including Arbitrary Couplings*, **sharc-md.org**, 2019.
22 J. C. Tully, *J. Chem. Phys.*, 1990, **93**, 1061–1071.
23 G. Granucci, M. Persico and A. Zoccante, *J. Chem. Phys.*, 2010, **133**, 134111–134119.
24 L. P. Dempsey, C. Murray, P. A. Cleary and M. I. Lester, *Phys. Chem. Chem. Phys.*, 2008, **10**, 1424–1432.